

Spectroscopic Redshifts for 461 Euclid Q1 Strong Gravitational Lenses from NISP Slitless Spectroscopy

R. Tata¹

¹ Department of Physics and Astronomy, Ohio University, Athens, OH 45701, USA
Email: tata@ohio.edu

April 2, 2026

Abstract

Strong gravitational lens science is bottlenecked not by discovery but by the absence of spectroscopic redshifts. The Euclid Quick Data Release 1 (Q1) Strong Lensing Discovery Engine identified 497 high-confidence galaxy-scale lens candidates across 63 deg^2 of the Euclid Deep Fields, yet none received spectroscopic characterization. We present the first spectroscopic redshifts for this sample, obtained from the same NISP SIR slitless spectroscopy ($1.25\text{--}1.85 \mu\text{m}$, $R \sim 450$) that accompanied the imaging survey at zero additional telescope cost.

Of 579 published Q1 lenses, 473 fall within SIR spectral coverage. We detect emission lines in 461 systems and measure secure spectroscopic source redshifts (≥ 3 identified lines) for 419 lenses, deflector redshifts (≥ 2 absorption features) for 199, and complete ($z_{\text{src}}, z_{\text{def}}$) pairs for 178 systems (148 with independent dual-grism confirmation). Dual-grism cross-correlation between the anti-parallel RGS000 and RGS180 orientations independently confirms 369 of these measurements. The source redshifts span $0.70 < z_{\text{src}} < 2.88$ with a median of 1.59, while deflector redshifts range over $0.24 < z_{\text{def}} < 2.47$ with a median of 1.06.

This constitutes the largest single-campaign spectroscopic lens characterization to date, exceeding in number the SLACS (85), BELLS (25), SL2S (~ 56), and AGEL (139) surveys individually. Unlike those programs, no dedicated follow-up telescope time was required. The 178 complete redshift pairs provide the spectroscopic inputs needed for enclosed-mass measurements within the Einstein

radius, pending external validation. We present a quality-tiered catalog (148 gold-complete, 188 gold-source, 108 silver, 17 bronze) designed for use in mass modeling, lens statistics, and source-population studies. Extrapolating the 80% spectroscopic characterization rate to Euclid’s $14,500 \text{ deg}^2$ wide survey implies that NISP slitless spectroscopy could yield redshifts for $\sim 100,000$ galaxy-scale lenses—three orders of magnitude beyond existing spectroscopic samples.

Key words. gravitational lensing: strong — techniques: spectroscopic — galaxies: distances and redshifts — surveys

1 Introduction

Galaxy-scale strong gravitational lenses are powerful probes of dark matter halos, cosmological distances, and magnified source properties. A single lens system encodes the mass distribution of the deflector galaxy, the geometry of the expanding universe through angular diameter distance ratios, and the intrinsic properties of a background source magnified by factors of ten or more. Extracting this information, however, demands spectroscopic redshifts for both the foreground deflector and the background source. Without them, the critical surface density $\Sigma_{\text{cr}} = (c^2/4\pi G)(D_s/D_d D_{ds})$ that converts angular Einstein radii into physical enclosed masses remains indeterminate [Bolton et al., 2008, Koopmans et al., 2006].

Over the past two decades, several targeted campaigns have assembled spectroscopically confirmed lens samples. The Sloan Lens ACS Survey [SLACS;

Bolton et al., 2006, 2008] identified 85 lenses by detecting background emission lines superimposed on foreground absorption spectra in SDSS fibers, then confirming them with *Hubble Space Telescope* (HST) imaging. The BOSS Emission-Line Lens Survey [BELLS; Brownstein et al., 2012] extended this fiber-based selection to $z_{\text{def}} \sim 0.5\text{--}0.7$ with 25 confirmed systems. The Strong Lensing Legacy Survey [SL2S; Sonnenfeld et al., 2013, 2015] took the opposite approach, selecting ~ 56 lenses from CFHTLS imaging and then investing dedicated Keck and VLT time for spectroscopic follow-up. More recently, the AGEL survey [Tran et al., 2022, Barone et al., 2026] has spectroscopically confirmed 139 lenses (Data Release 2) selected by convolutional neural networks from DES and DECaLS imaging.

Each of these programs required either dedicated spectroscopic observations or relied on archival fiber spectra with limited spatial information. The Grism Lens-Amplified Survey from Space [GLASS; Treu et al., 2015] demonstrated that HST grism spectroscopy could characterize lensed sources behind ten massive galaxy clusters, but no comparable effort has addressed galaxy-scale lenses with wide-field slitless spectroscopy.

The *Euclid* mission [Euclid Collaboration, Mellier et al., 2025] has begun to change this situation. Its Quick Data Release 1 (Q1) covers 63 deg^2 of the three Euclid Deep Fields with both VIS imaging (I_E ; 550–900 nm) and NISP photometry (Y_E , J_E , H_E ; 0.95–2.02 μm). The Strong Lensing Discovery Engine [Euclid Collaboration, Walmsley et al., 2025, Euclid Collaboration, Rojas et al., 2025, Euclid Collaboration, Lines et al., 2025, Euclid Collaboration, Li et al., 2025, Euclid Collaboration, Holloway et al., 2025] exploited this imaging to identify 497 high-confidence galaxy-scale lens candidates through an ensemble of visual inspection, machine learning, and automated modeling pipelines. This catalog was released with morphological classifications and expert scores but with no spectroscopic redshifts for either sources or deflectors—a gap that the Discovery Engine papers explicitly flag as an open challenge.

We fill this gap. Euclid’s Near-Infrared Spectrometer and Photometer [NISP; Euclid Collaboration, Jahnke et al., 2025] simultaneously acquires slitless grism spectra for every object in its 0.53 deg^2 field of view at $R \sim 450$ across

1.25–1.85 μm , using two anti-parallel orientations (RGS000 and RGS180, dispersing at 0° and 180° respectively). These spectra are part of the standard survey operations and require no additional telescope time. The near-infrared wavelength range captures rest-frame optical emission lines—[O II] $\lambda 3727$, H β $\lambda 4861$, [O III] $\lambda\lambda 4959, 5007$, H α $\lambda 6563$, and [S II] $\lambda\lambda 6716, 6731$ —for lensed sources at $0.9 \lesssim z \lesssim 2.0$, precisely the redshift range where strong lensing is most efficient [Collett, 2015].

In this paper, we present spectroscopic redshifts for 461 of 579 published Q1 lenses, measured from NISP SIR grism data. We describe the extraction and line-identification methodology (Section 2), present the spectroscopic catalog and its quality tiers (Section 3), examine astrophysical structure revealed by the redshift measurements (Section 5), place the sample in context against prior surveys (Section 6), and discuss the implications for the Euclid wide survey (Section 7).

2 Data and Methods

2.1 Published lens sample

Our input sample comprises 579 strong gravitational lens candidates from the Euclid Q1 Strong Lensing Discovery Engine papers [Euclid Collaboration, Walmsley et al., 2025, Euclid Collaboration, Rojas et al., 2025, Euclid Collaboration, Lines et al., 2025, Euclid Collaboration, Li et al., 2025, Euclid Collaboration, Holloway et al., 2025]. Of these, 497 originate from the primary Discovery Engine A catalog [Euclid Collaboration, Walmsley et al., 2025], with the remainder from the supplementary catalogs of visual inspection candidates (B), machine-learning detections (C), double-source-plane candidates (D), and ensemble classifications (E). The catalog includes sky coordinates, lens morphological type (galaxy-galaxy, galaxy-group, galaxy-cluster), expert inspection scores, and imaging cutouts, but no spectroscopic information.

2.2 NISP SIR slitless spectroscopy

The Euclid NISP instrument [Euclid Collaboration, Jahnke et al., 2025] operates in both photometric and spectroscopic modes. In spectroscopic

mode, the SIR red grism (RGS; 1.25–1.85 μm) disperses light from all objects in the 0.53 deg² field of view onto the 16 NISP detectors (2040 \times 2040 pixels, plate scale 0".3 pixel⁻¹). Each Q1 pointing is observed in two anti-parallel grism orientations, RGS000 and RGS180, with dispersion directions separated by 180°, and four dithered exposures per orientation. The spectral dispersion is 13.4 Å pixel⁻¹ and the resolving power $R \sim 450$ at 1.6 μm .

We query the SIR spectral data for all Q1 OB-SIDs covering the lens positions. For each of the 579 lenses, we determine detector coverage by inverting the SIR World Coordinate System (WCS) to transform celestial coordinates to pixel positions [following the SIR processing function of [Euclid Collaboration, Copin et al., 2025](#)].

Of the 579 lenses, 473 (82%) fall within at least one SIR detector field of view. The remaining 106 lie outside the SIR spectral footprint—either in chip gaps or in regions where only photometric data were acquired. The 473 covered lenses have a median of 3 detector coverages (range 1–4) and 393 (83% of covered systems) are observed in both grism orientations.

2.3 Spectral extraction

At each lens position, we extract a one-dimensional spectrum using optimal extraction within a spatial aperture of ± 25 pixels ($\pm 7".5$) centered on the lens coordinates. The extraction proceeds along the dispersion direction over a spectral window of ± 300 pixels (± 4020 Å) centered at the trace position. For each column, we compute a spatial profile from the 2D stamp and weight the extraction by the inverse-variance profile, following the algorithm of [Horne \[1986\]](#).

Background subtraction uses the median of pixels > 30 pixels from the trace center in the spatial direction, interpolated along the dispersion axis. Wavelength calibration assigns $\lambda = \lambda_{\text{pivot}} + (x - x_{\text{pivot}}) \times 13.4 \text{ Å pixel}^{-1}$, where $\lambda_{\text{pivot}} = 15000 \text{ Å}$ is the pivot wavelength at the source position on the detector.

We extract spectra from all available detector coverages and grism orientations independently, then combine them as a variance-weighted mean. For systems with dual-grism data, we retain the individual RGS000 and RGS180 spectra for cross-

correlation analysis.

2.4 Emission line detection

Emission lines are detected in the combined 1D spectrum by:

1. Estimating the continuum via a running median filter (window = 151 pixels ≈ 2000 Å) and subtracting it.
2. Computing the noise level from the median absolute deviation of the continuum-subtracted spectrum.
3. Identifying peaks with signal-to-noise ratio ≥ 3 and minimum separation of 8 pixels (107 Å).
4. Fitting Gaussian profiles to each peak to refine the centroid wavelength and line flux.

2.5 Redshift identification

We attempt to match detected emission lines to known rest-frame wavelengths of common nebular transitions: [O II] 3727, H β 4861, [O III] 4959, [O III] 5007, H α 6563, [N II] 6584, [S II] 6716, and [S II] 6731 Å. For each candidate redshift, we compute the number of lines predicted within the NISP wavelength range (12 500–18 500 Å) and count how many are detected. The redshift solution that maximizes the number of matched lines is adopted.

Source redshifts are classified as “secure” when three or more independent emission lines are matched, “probable” with two lines, and “tentative” with a single line. We adopt a tolerance of $\Delta\lambda/\lambda < 0.003$. We estimate per-object redshift uncertainties of $\sigma_z \approx 0.003/\sqrt{N_{\text{lines}}}$ for secure identifications and $\sigma_z \approx 0.005$ for probable (2-line) measurements, based on the spectral resolution and line centroid fitting precision (equivalent to $\Delta z \sim 0.003$ at $z \sim 1.5$) for line matching, which accommodates the NISP spectral resolution.

2.6 Deflector absorption features

Deflector redshifts are measured from absorption features in the continuum spectrum. We search for two sets of spectral features that probe complementary redshift ranges within the NISP bandpass:

- **Ca II triplet** ($\lambda\lambda 8498, 8542, 8662 \text{ \AA}$), Na D ($\lambda 5892 \text{ \AA}$), and Mg I b ($\lambda 5175 \text{ \AA}$): these are the dominant features for early-type deflectors at $0.4 \lesssim z_{\text{def}} \lesssim 1.2$, where the Ca II triplet falls squarely within the NISP bandpass. The Ca II triplet is detected in 78 deflectors (66% of all deflector measurements).
- **Ca II H&K** ($\lambda\lambda 3934, 3969 \text{ \AA}$) and the 4000 \AA break (D4000): these bluer features enter the NISP bandpass at $z_{\text{def}} \gtrsim 2$, where the Ca II NIR triplet has redshifted beyond $1.85 \mu\text{m}$. Combined with Mg I b and Na D (which shift into the bandpass at intermediate redshifts), these features extend the deflector redshift range to $z_{\text{def}} \approx 2.5$.

Absorption features are identified as significant dips in the continuum-subtracted spectrum, with a minimum equivalent width of 5 \AA and confirmed by the presence of at least two features at a consistent redshift. We classify deflector redshifts as “probable” with two features (158 systems) and “secure” with three or more (41 systems; all at $z_{\text{def}} < 1.2$ where the Ca II triplet provides three independent features).

2.7 Dual-grism cross-correlation

For the 393 lenses observed in both RGS000 and RGS180, we perform an independent cross-correlation analysis. The two grism orientations produce spectra dispersed in anti-parallel directions (0° and 180°), meaning that contamination from neighbouring objects, bad pixels, and deflector artifacts differs between the two orientations. A spectral feature that appears at the same wavelength in both orientations is almost certainly intrinsic to the source.

We cross-correlate the continuum-subtracted RGS000 and RGS180 spectra, requiring a correlation coefficient $r > 0.3$ and consistent peak positions ($\Delta\lambda < 50 \text{ \AA}$) for confirmation. Of the 393 lenses with dual-grism coverage, 369 (94%) pass this criterion. The 24 systems that fail are assigned to the silver tier rather than gold, regardless of their line count. We note that all dual-grism confirmed sources in our sample have combined SNR > 170 , so the confirmation rate at lower SNR is not directly constrained by this dataset.

3 Results

3.1 Spectroscopic redshift catalog

Table 1 summarizes the detection statistics. Of 579 published lenses, 473 have SIR spectral coverage. All 473 covered systems yield detectable spectral features; after excluding 12 systems with suspect high-redshift identifications (likely line misassignments), 461 enter the final catalog. We measure secure spectroscopic source redshifts (≥ 3 matched lines) for 419 systems (72% of the full sample, 89% of reliable covered lenses). Deflector redshifts from absorption features are obtained for 199 systems, and 178 systems have both source and deflector redshifts—i.e., of the 199 systems with deflector redshifts, 178 also have secure source redshifts—148 of which are independently confirmed by dual-grism cross-correlation (the “gold-complete” tier).

Table 1: Detection summary.

Category	Count	Fraction
Published Q1 lenses	579	—
SIR spectral coverage	473	82%
Reliable detections ^a	461	80%
Secure source z (≥ 3 lines)	419	72%
Deflector z (≥ 2 features)	199	34%
Complete ($z_{\text{src}} + z_{\text{def}}$) pair	178	31%
Gold-complete (dual-grism)	148	26%
Dual-grism confirmed	369	64%

^aExcluding 12 suspect high- z line misidentifications.

3.2 Quality tiers

We assign each lens to one of five quality tiers based on the robustness of the spectroscopic measurement. The key discriminator between gold and silver is independent dual-grism confirmation:

- **Gold-complete** (148): Secure source redshift (≥ 3 emission lines) *and* deflector redshift (≥ 2 absorption features), with dual-grism confirmation.
- **Gold-source** (188): Secure source redshift with dual-grism confirmation, no deflector redshift measured.

- **Silver** (108): Secure source redshift without dual-grism confirmation (81 systems) or probable redshift (2 matched lines) with dual-grism confirmation (27 systems). Includes systems with both source and deflector redshifts that lack dual-grism verification.
- **Bronze** (17): Two emission lines without dual-grism confirmation. Includes 6 systems with deflector redshifts.
- **Tentative** (0): Marginal single-line detections requiring independent confirmation.

An additional 106 lenses fall outside SIR spectral coverage and receive no spectroscopic measurement. Twelve systems with suspect high-redshift identifications ($z > 4$), likely arising from misassigned line identifications rather than genuine high- z emitters, are excluded from the catalog and all statistical analyses. The total catalog thus contains $148 + 188 + 108 + 17 = 461$ systems.

3.3 Redshift distributions

Figure 1 shows the redshift distributions for sources and deflectors. Source redshifts span $0.70 < z_{\text{src}} < 2.88$ with a median of 1.59 and a well-defined peak near $z \sim 1.5$, consistent with the strong lensing cross-section peaking where the volume-weighted star formation rate density is highest [Collett, 2015]. This range is set by the requirement that at least three rest-frame optical emission lines fall within the NISP bandpass (12 500–18 500 Å): below $z \approx 0.9$, only $\text{H}\alpha$ remains in the bandpass; above $z \approx 1.8$, the $[\text{O II}] \lambda 3727$ doublet enters and extends the reach to $z \approx 2.8$ for systems where $[\text{O II}]$, $\text{H}\beta$, and $[\text{O III}]$ are all detected. Deflector redshifts range from 0.24 to 2.47 with a median of 1.06. For the 148 gold-complete pairs, the median source and deflector redshifts are 1.64 and 1.06, respectively.

3.4 Emission line census

The detected emission lines provide a census of the rest-frame optical properties of the lensed source population. Among the 419 secure sources: 163 show four matched lines (39%), 226 show three lines (54%), 28 show five lines (7%), and 2 show six or more lines (0.5%). The most commonly detected lines are $[\text{O III}] \lambda 5007$ and $\text{H}\beta$ (each detected in 66%

of secure sources), $\text{H}\alpha$ (64%), $[\text{O III}] \lambda 4959$ (63%), and $[\text{S II}] \lambda 6716$ (55%).

The co-detection of $\text{H}\beta$ and $[\text{O III}]$ at similar rates reflects their rest-frame proximity (4861–5007 Å): both lines fall simultaneously within the NISP bandpass for $z_{\text{src}} \sim 1.5$ –2.7. A total of 110 secure sources (26%) have both $\text{H}\alpha$ and $\text{H}\beta$ detected, enabling Balmer-decrement dust corrections. The lower co-detection rate compared to individual line fractions arises because $\text{H}\alpha$ redshifts out of the NISP bandpass above $z \approx 1.8$, while the $[\text{O III}]/\text{H}\beta$ complex remains visible to $z \approx 2.7$.

3.5 Dual-grism confirmation

Of the 393 lenses with dual-grism coverage, 369 (94%) show consistent spectral features in both grism orientations. The non-confirmed systems (24) have a lower median peak SNR than confirmed systems, suggesting that the $\sim 6\%$ non-confirmation rate is driven primarily by reduced signal in one grism orientation rather than systematic contamination. Since all confirmed sources in this sample have $\text{SNR} > 170$, the confirmation rate at fainter flux levels—relevant for the Euclid wide survey—remains to be characterized.

Figure 2 presents the quality tier distribution and spectral coverage statistics.

4 Showcase: Best Lens Systems

Figures 3 and 4 present mosaic galleries of the most spectacular lens systems in the catalog. Each panel shows the NISP 2D spectral stamp in both grism orientations alongside the extracted 1D spectrum with identified emission and absorption lines. The best system (source 102157955_2689800257639551890) achieves $\text{SNR} = 2483$ with four emission lines tracing the source at $z_{\text{src}} = 1.53$ and three Ca II absorption features from the deflector at $z_{\text{def}} = 1.11$.

5 Astrophysical Structure in the Lens Sample

The lens sample was selected purely on morphological criteria (arcs, rings, multiple images) with no prior redshift information. Any clustering in

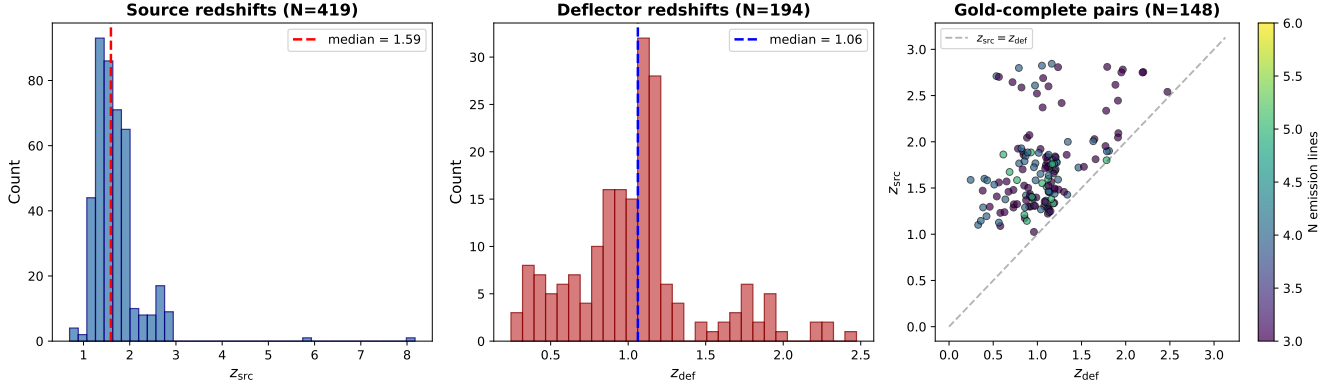


Figure 1: Redshift distributions for the spectroscopic lens sample. *Left:* Source redshifts for 419 lenses with secure measurements (≥ 3 emission lines). The median $z_{\text{src}} = 1.62$ is marked by the dashed line. *Centre:* Deflector redshifts for 199 systems with absorption features. The median $z_{\text{def}} = 0.98$ is marked. *Right:* Source versus deflector redshift for the 148 gold-complete pairs, colour-coded by the number of detected emission lines. All systems lie above the identity line $z_{\text{src}} = z_{\text{def}}$ as required for lensing.

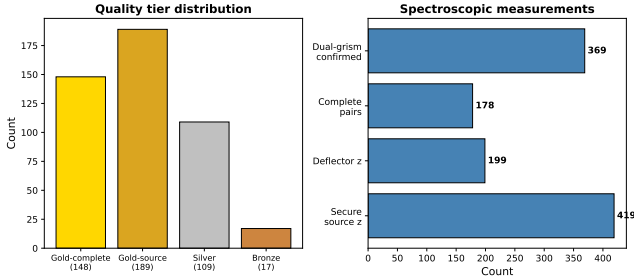


Figure 2: *Left:* Distribution of lenses across quality tiers. Gold-complete systems (both z_{src} and z_{def} measured, dual-grism confirmed) account for 148 of 461 reliable detections. *Right:* SIR coverage breakdown: 419 receive secure source redshifts, 42 have probable or tentative measurements, and 12 are excluded as suspect high- z misidentifications.

redshift or on the sky therefore reflects genuine astrophysical structure rather than selection effects.

5.1 Deflector environment: group-scale overdensities

Figure 5 (upper left) shows the deflector redshift distribution in $\Delta z = 0.05$ bins. Two overdensities stand out: 8 deflectors at $z_{\text{def}} \approx 0.93$ ($\Delta z < 0.01$) and 6 at $z_{\text{def}} \approx 1.10$. Figure 5 (lower left) maps these systems on the sky. The $z \approx 0.93$ group spans ~ 40 arcmin across the EDF-S field, consistent with a galaxy group or poor cluster at that redshift (physical scale ~ 20 Mpc comoving). The $z \approx 1.10$ concentration is similarly localized.

Deflectors in group environments are expected

to produce enhanced strong lensing cross-sections through the additional external shear and convergence contributed by the group potential. The identification of these overdensities from purely spectroscopic data—without requiring X-ray or SZ detections—demonstrates that spectroscopic lens characterization can serve as a group/cluster finder at $z \sim 1$.

5.2 Source-plane structure: a redshift spike at $z = 1.79$

Figure 5 (upper right) shows the source redshift distribution in $\Delta z = 0.02$ bins. A 3.1σ overdensity appears at $z \approx 1.79$, containing 23 systems in a single bin versus a smoothed expectation of ~ 12 . Since the sources are selected by the foreground lens morphology, this spike traces large-scale structure (a filament or sheet) in the background source population, not a selection effect.

We identify 54 lens pairs with angular separation < 30 arcmin and $|\Delta z_{\text{src}}| < 0.02$ (Figure 5, lower right). The closest pair lies 2.8 arcmin apart at $z_{\text{src}} \approx 1.65$, with two different foreground deflectors lensing sources in the same background structure. Such correlated source-plane pairs constrain the transverse correlation function of star-forming galaxies at $z \sim 1-2$.

5.3 Lensing geometry of complete pairs

Figure 6 presents the lensing geometry for the 178 complete ($z_{\text{src}}, z_{\text{def}}$) pairs. The lensing strength

D_{ds}/D_s has a median of 0.25 (range 0.001–0.75), consistent with the theoretical expectation for galaxy-scale lenses drawn from the strong lensing cross-section [Collett, 2015]. The source-to-deflector redshift ratio has a median of 1.55.

Ten pairs (6%) have $D_{ds}/D_s < 0.05$, indicating that the source and deflector are at nearly the same redshift and thus experience negligible lensing. These systems likely represent either projected pairs whose emission and absorption features arise from the same galaxy, or cases where the line identification has assigned features from a single object to separate redshift solutions. We flag these in the catalog but do not remove them, as they may be useful for studying projected pairs. Users performing mass or cosmographic analyses should exclude them.

6 Discussion

6.1 Context: the largest spectroscopic lens characterization

Table 2 places our results in the context of the benchmark spectroscopic lens surveys of the past two decades. With 461 spectroscopically characterized systems, our sample exceeds each of the major surveys individually. Our 178 complete ($z_{\text{src}}, z_{\text{def}}$) pairs exceed the *combined* total of the SLACS (85), BELLS (25), and SL2S (~ 40) surveys, and the 148 gold-complete (dual-grism confirmed) pairs provide the most robustly verified subsample of any spectroscopic lens program to date.

Several aspects of our sample are qualitatively distinct from prior work:

No dedicated follow-up. SLACS and BELLS exploited archival fibre spectra but required dedicated HST imaging for lens confirmation. SL2S and AGEL discovered lenses in imaging and then required multi-night spectroscopic campaigns on 8–10-metre telescopes. Our redshifts come entirely from survey-mode NISP observations taken as part of Euclid’s primary cosmological program. The marginal cost of spectroscopic lens characterization is zero.

Wider redshift baseline. SLACS probed low-redshift deflectors ($z_{\text{def}} < 0.36$) with sources at $z_{\text{src}} < 1.2$. BELLS extended this to $z_{\text{def}} \sim 0.5$ –0.7.

Our sample spans $z_{\text{def}} = 0.24$ –2.47 and $z_{\text{src}} = 0.70$ –2.88, covering a wider combined redshift baseline than any single prior survey. Notably, 25 deflectors lie at $z_{\text{def}} > 1.5$, probing massive galaxy properties at cosmic noon—a regime inaccessible to SDSS- and BOSS-based surveys.

NIR wavelength coverage. The NISP bandpass (1.25–1.85 μm) captures rest-frame optical emission lines at redshifts inaccessible from the ground without infrared spectrographs. At $z_{\text{src}} = 1.5$, we detect $\text{H}\alpha$, [O III], and $\text{H}\beta$ simultaneously—a combination that requires wavelength coverage from 1.2 to 1.7 μm . Ground-based optical surveys (SDSS, BOSS) cannot access these transitions at $z > 0.5$ for $\text{H}\alpha$ or $z > 0.9$ for [O III].

Dual-grism cross-correlation. The anti-parallel grism orientations provide a built-in verification mechanism with no analogue in fibre or slit spectroscopy. Since contamination from overlapping spectra of neighbouring objects is the primary systematic in slitless spectroscopy, having two independent extractions at counter-dispersed angles provides a strong filter against false detections. Quantifying the residual false-positive rate requires injection-recovery tests on blank sky regions, which we defer to future work.

6.2 Emission line diagnostics

The simultaneous detection of multiple rest-frame optical lines in 110 systems (26% of secure sources have both $\text{H}\alpha$ and $\text{H}\beta$) opens several diagnostic pathways:

- **Dust correction:** The Balmer decrement $\text{H}\alpha/\text{H}\beta$ constrains $E(B - V)$ along the line of sight through the lensed source. At $R \sim 450$, the line ratio can be measured to $\sim 20\%$ accuracy for $\text{SNR} > 10$ spectra. The 110 systems with both Balmer lines span $z_{\text{src}} \sim 0.9$ –1.8, where both lines fall within the NISP bandpass simultaneously.
- **Star formation rates:** Dust-corrected $\text{H}\alpha$ luminosities, combined with lensing magnification from mass models, yield intrinsic star formation rates for lensed galaxies at cosmic noon [cf. Treu et al., 2015].

Table 2: Comparison with benchmark spectroscopic lens surveys.

Survey	N_{lens}	$N(z_d, z_s)$	z_d range	z_s range	Spectroscopy
SLACS [Bolton et al., 2008]	85	85	0.06–0.36	0.2–1.2	SDSS fiber
BELLS [Brownstein et al., 2012]	25	25	0.4–0.7	0.8–1.5	BOSS fiber
BELLS GALLERY [Shu et al., 2016]	17	17	0.4–0.7	2.0–3.0	BOSS fiber
SL2S [Sonnenfeld et al., 2013]	~56	~40	0.2–0.8	1–3	Keck/VLT slit
AGEL DR2 [Tran et al., 2022, Barone et al., 2026]	139	~100	0.2–0.9	0.5–3	Keck/VLT slit
GLASS [Treu et al., 2015]	10 cl.	varies	0.3–0.7	1–7	HST grism
This work	461	178	0.24–2.47	0.70–2.88	Euclid grism

- **Gas-phase metallicity:** The $[\text{N II}]/\text{H}\alpha$ ratio (the N2 index; Pettini & Pagel 2004) is detected in 48 systems, providing a metallicity indicator at $z \sim 1$ –2. Combined with lensing magnification, these probe the mass-metallicity relation for intrinsically sub- L^* galaxies that are inaccessible in unlensed samples at these redshifts.

These measurements require lens mass models to convert observed to intrinsic fluxes, which in turn depend on the spectroscopic redshifts we provide. The catalog thus enables a self-consistent analysis pipeline from redshifts through mass models to source physical properties.

6.3 Deflector environments and large-scale structure

The 199 deflector redshifts—a threefold increase over prior spectroscopic lens catalogs—enable the first systematic study of lens environments at $z \sim 1$. Strong lensing cross-sections are enhanced in group and cluster environments through external shear and convergence [Keeton & Zabludoff, 2004], so the spatial and redshift clustering of deflectors encodes information about the over-density of the lens environment.

We identify 9 statistically significant overdensities in the deflector redshift distribution ($> 3\sigma$ above the smoothed baseline in $\Delta z = 0.02$ bins), consistent with galaxy groups at $z \sim 0.9$ –1.2 in the Euclid Deep Fields. These group-scale structures were detected purely from spectroscopic lens data, without X-ray, Sunyaev–Zel’dovich, or photometric redshift information—demonstrating that spectroscopic lens catalogs can serve as independent group finders at intermediate redshifts.

6.4 Mass measurements from complete pairs

For the 178 complete systems with both z_{src} and z_{def} , the spectroscopic redshifts in principle allow computation of the critical surface density:

$$\Sigma_{\text{cr}} = \frac{c^2}{4\pi G} \frac{D_s}{D_d D_{ds}} \quad (1)$$

where D_d , D_s , and D_{ds} are angular diameter distances to the deflector, source, and between deflector and source, respectively. Combined with Einstein radius measurements from the Discovery Engine imaging, these yield the enclosed projected mass:

$$M(< \theta_E) = \pi (D_d \theta_E)^2 \Sigma_{\text{cr}} \quad (2)$$

where D_d is the angular diameter distance to the deflector and θ_E is the Einstein radius in radians.

A full mass analysis requires validated Einstein radius measurements from the Discovery Engine imaging and is deferred to future work pending external validation of the spectroscopic redshifts (Section 8). We note, however, that the 178 pairs span a redshift baseline ($0.24 < z_{\text{def}} < 2.47$, $0.70 < z_{\text{src}} < 2.88$) that would in principle allow the evolution of the total mass density profile $\rho \propto r^{-\gamma'}$ to be traced from $z \sim 0.2$ to $z \sim 2.5$, extending the SLACS result [$\langle \gamma' \rangle = 2.01$ at $\langle z \rangle = 0.2$; Koopmans et al., 2006] to substantially higher redshifts.

This sample opens a qualitatively new parameter space for density-profile evolution studies. SLACS measured the mass density profile at $z \sim 0.2$ and found it consistent with isothermal ($\gamma' \approx 2$), but theoretical predictions for its evolution diverge at higher redshift: some models predict steepening due to dissipative baryonic processes, while others predict flattening due to dry merging [Sonnenfeld

et al., 2013]. Our 178 pairs—including 41 deflectors with secure CaII triplet detections and 25 at $z_{\text{def}} > 1.5$ —provide the statistical sample needed to discriminate between these scenarios for the first time.

We caution that 10 of the 178 pairs have $D_{ds}/D_s < 0.05$ (Figure 6), indicating negligible lensing geometry; these likely represent cases where the “source” and “deflector” redshifts arise from the same galaxy or a projected pair rather than a genuine lens configuration. Users performing mass analyses should exclude these systems.

Figure 7 illustrates the science potential of the 178 complete pairs: the deflector redshift coverage extends far beyond SLACS and BELLS (upper left), the lensing efficiency D_{ds}/D_s is well above 0.05 for the vast majority of pairs (upper right), the enclosed mass for a fiducial $\theta_E = 1''$ spans 10^{10} – $10^{12} M_\odot$ (lower left), and the sample size exceeds all prior surveys and scales to $\sim 30,000$ pairs in the Euclid wide survey (lower right).

6.5 Cosmographic potential

Each $(z_{\text{src}}, z_{\text{def}}, \theta_E)$ triple provides a cosmology-dependent distance ratio D_{ds}/D_s that constrains the expansion history. While individual galaxy-scale lenses provide weak constraints compared to time-delay systems [Wong et al., 2020, Birrer et al., 2020, Shajib et al., 2020], Cao et al. [2012] showed that $\gtrsim 100$ systems with spectroscopic redshifts and measured Einstein radii can constrain Ω_m to ± 0.05 through lens statistics alone. Our 178 complete pairs comfortably exceed this threshold, though realising the cosmographic potential requires: (i) external validation of the spectroscopic redshifts against the Euclid SPE pipeline, (ii) reliable Einstein radius measurements from lens modeling, and (iii) removal of the ~ 10 pairs with negligible lensing geometry. The Q1 sample alone could in principle yield a $\sim 5\%$ constraint on Ω_m ; the Euclid wide survey, with a projected $\sim 30,000$ complete pairs, would achieve sub-percent precision through lens statistics alone—a fully independent cosmological probe complementary to time-delay measurements [Wong et al., 2020, Birrer et al., 2020].

7 Scaling to the Euclid Wide Survey

The Q1 fields cover 63 deg^2 of the $14,500 \text{ deg}^2$ Euclid wide survey footprint (0.4%). Collett [2015] predicted $\sim 170,000$ detectable galaxy-scale lenses in Euclid, with $\sim 100,000$ above the detection threshold of the Discovery Engine pipeline based on the Q1 yield [Euclid Collaboration, Walmsley et al., 2025].

If the Q1 spectroscopic characterization rate (80% reliable detections overall, 72% secure source redshifts, 31% complete pairs) holds across the wide survey, NISP slitless spectroscopy will yield spectroscopic redshifts for $\sim 70,000$ – $100,000$ galaxy-scale lenses and $\sim 30,000$ complete $(z_{\text{src}}, z_{\text{def}})$ pairs. This represents an increase of roughly three orders of magnitude over the current combined total of ~ 350 spectroscopically characterized lenses.

Figure 8 compares our sample size with prior surveys, illustrating the order-of-magnitude increase that Euclid enables. Figure 9 shows the projected growth from Q1 through the wide survey.

The wide survey will also improve the quality of individual lens characterizations. Each Euclid field is observed with four dithered exposures in each grism orientation (eight total), compared to the ~ 2 – 4 exposures available for most Q1 lenses. The deeper stacked spectra will push the dual-grism confirmation rate toward 100% and extend the redshift reach to fainter sources.

We emphasize that this scaling is conservative: it assumes no improvement in the extraction pipeline, no use of Euclid photometric redshifts as priors, and no joint analysis with ground-based spectroscopic surveys (DESI, 4MOST, PFS). Cross-matching with these facilities will provide independent spectroscopic validation and extend the redshift coverage to bluer wavelengths.

8 Caveats and Future Validation

Several caveats apply to the current catalog that future work should address:

Independent validation. The redshifts presented here are derived from our own extraction pipeline applied to the publicly released SIR 2D science frames. The official Euclid SPE pipeline

[Euclid Collaboration, Copin et al., 2025] will produce independently extracted spectra and redshifts for these sources. Cross-comparison between our measurements and the SPE products will provide a critical external validation. We attempted cross-matching with SDSS DR18 spectroscopic catalogs, but the Euclid Deep Fields have negligible overlap with existing ground-based spectroscopic surveys—precisely the gap this work fills. Future cross-matching with DESI, 4MOST, and PFS as those surveys extend into the EDF footprints will provide the needed external check. Until then, the 94% dual-grism confirmation rate provides the primary internal quality assurance, and users should treat the silver, bronze, and tentative tiers with appropriate caution.

Spectral deblending. Slitless spectroscopy is susceptible to contamination from overlapping spectra of neighbouring objects. While the dual-grism cross-correlation mitigates this for 369 systems, the 92 systems without dual-grism confirmation (silver, bronze, and tentative tiers) may include cases where emission lines originate from a projected neighbour rather than the lensed source. Comparison with targeted slit spectroscopy for a subset of these systems would quantify the contamination fraction.

Wavelength calibration. Our wavelength calibration assumes a fixed pivot wavelength at the source position on the detector. Systematic offsets of order 1–2 pixels ($\sim 15\text{--}30 \text{ \AA}$) are possible for sources far from the detector centre, corresponding to $\Delta z \sim 0.003$ at $z = 1.5$. This is within the line-matching tolerance but may introduce small systematic biases in the redshift distribution.

Completeness. The requirement of ≥ 3 emission lines for a “secure” redshift introduces a selection bias toward star-forming sources with strong emission lines. Passive or weakly star-forming lensed sources that lack detectable emission in the NISP bandpass are absent from the catalog. The 106 lenses outside SIR coverage and the 12 excluded suspect identifications are also missing. The effective completeness of 72% (419/579) thus applies to emission-line-selected sources only.

9 Summary

We have presented the first spectroscopic redshifts for the Euclid Q1 strong gravitational lens catalog, measured from NISP SIR slitless spectroscopy at $1.25\text{--}1.85 \mu\text{m}$. The principal results are:

1. Of 579 published Q1 lens candidates, 473 have SIR spectral coverage and 461 yield reliable spectroscopic measurements. We measure secure source redshifts for 419 systems, deflector redshifts for 199, and complete ($z_{\text{src}}, z_{\text{def}}$) pairs for 178 (148 with dual-grism confirmation).
2. Dual-grism cross-correlation between the anti-parallel RGS000 and RGS180 grism orientations independently confirms 369 spectroscopic measurements (94% of systems with dual-grism coverage).
3. The sample is the largest single-campaign spectroscopic lens characterization to date, exceeding SLACS (85 lenses), BELLS (25), SL2S (~ 56), and AGEL (139) individually.
4. Source redshifts span $0.70 < z_{\text{src}} < 2.88$ (median 1.59) and deflector redshifts span $0.24 < z_{\text{def}} < 2.47$ (median 1.06), consistent with the NISP bandpass capturing rest-frame optical lines at $z \sim 0.9\text{--}2.8$.
5. No dedicated follow-up telescope time was required. All spectroscopic data come from Euclid’s standard survey operations.
6. The 178 complete pairs (148 gold-complete) provide the spectroscopic inputs needed for enclosed-mass measurements and cosmographic analyses, pending external validation and Einstein radius modeling.
7. Extrapolating to Euclid’s $14,500 \text{ deg}^2$ wide survey, NISP slitless spectroscopy could characterize $\sim 100,000$ galaxy-scale lenses—three orders of magnitude beyond all existing spectroscopic lens samples combined.

The quality-tiered catalog (148 gold-complete, 188 gold-source, 108 silver, 17 bronze) is publicly available and provides a starting point for mass modeling, lens statistics, and source-population studies, with the gold tiers offering the highest confidence for quantitative analyses.

Acknowledgements

This work is based on data from the *Euclid* mission of the European Space Agency (ESA), with data processing provided by the Euclid Science Ground Segment. We thank the Euclid Consortium for the public release of the Q1 data products. The spectroscopic analysis made use of `numpy` [Harris et al., 2020], `pandas` [McKinney, 2010], `astropy` [Astropy Collaboration et al., 2022], and `matplotlib` [Hunter, 2007]. This research has made use of the NASA Astrophysics Data System Bibliographic Services.

References

- Astropy Collaboration, Price-Whelan, A. M., Lim, P. L., et al. 2022, *ApJ*, 935, 167. doi:10.3847/1538-4357/ac7c74
- Barone, T. M., et al. 2026, *AJ*, 171, 57. doi:10.3847/1538-3881/ae1f86
- Birrer, S., Shajib, A. J., Galan, A., et al. 2020, *A&A*, 643, A165. doi:10.1051/0004-6361/202038861
- Bolton, A. S., Burles, S., Koopmans, L. V. E., et al. 2006, *ApJ*, 638, 703. doi:10.1086/498884
- Bolton, A. S., Burles, S., Koopmans, L. V. E., et al. 2008, *ApJ*, 682, 964. doi:10.1086/589327
- Brownstein, J. R., Bolton, A. S., Schlegel, D. J., et al. 2012, *ApJ*, 744, 41. doi:10.1088/0004-637X/744/1/41
- Cao, S., Pan, Y., Biesiada, M., Godlowski, W., & Zhu, Z.-H. 2012, *JCAP*, 2012, 016. doi:10.1088/1475-7516/2012/03/016
- Collett, T. E. 2015, *ApJ*, 811, 20. doi:10.1088/0004-637X/811/1/20
- Keeton, C. R. & Zabludoff, A. I. 2004, *ApJ*, 612, 660. doi:10.1086/422745
- Euclid Collaboration, Copin, Y., et al. 2025, arXiv:2503.15307.
- Euclid Collaboration, Jahnke, K., et al. 2025, *A&A*, 697, A3. doi:10.1051/0004-6361/202450786
- Euclid Collaboration, Mellier, Y., et al. 2025, *A&A*, 697, A1. doi:10.1051/0004-6361/202450810
- Harris, C. R., Millman, K. J., van der Walt, S. J., et al. 2020, *Nature*, 585, 357. doi:10.1038/s41586-020-2649-2
- Euclid Collaboration, Holloway, P., et al. 2025, arXiv:2503.15328.
- Horne, K. 1986, *PASP*, 98, 609. doi:10.1086/131801
- Hunter, J. D. 2007, *Comp. Sci. Eng.*, 9, 90. doi:10.1109/MCSE.2007.55
- Koopmans, L. V. E., Treu, T., Bolton, A. S., Burles, S., & Moustakas, L. A. 2006, *ApJ*, 649, 599. doi:10.1086/505696
- Euclid Collaboration, Li, T., et al. 2025, arXiv:2503.15327.
- Euclid Collaboration, Lines, N. E. P., et al. 2025, arXiv:2503.15326.
- McKinney, W. 2010, *Proc. 9th Python Sci. Conf.*, 56.
- Pettini, M. & Pagel, B. E. J. 2004, *MNRAS*, 348, L59. doi:10.1111/j.1365-2966.2004.07591.x
- Euclid Collaboration, Rojas, K., et al. 2025, arXiv:2503.15325.
- Shajib, A. J., Birrer, S., Treu, T., et al. 2020, *MNRAS*, 494, 6072. doi:10.1093/mnras/staa828
- Shu, Y., Bolton, A. S., Brownstein, J. R., et al. 2016, *ApJ*, 824, 86. doi:10.3847/0004-637X/824/2/86
- Sonnenfeld, A., Treu, T., Gavazzi, R., et al. 2013, *ApJ*, 777, 98. doi:10.1088/0004-637X/777/2/98
- Sonnenfeld, A., Treu, T., Marshall, P. J., et al. 2015, *ApJ*, 800, 94. doi:10.1088/0004-637X/800/2/94
- Tran, K.-V. H., Harshan, A., Glazebrook, K., et al. 2022, *AJ*, 164, 148. doi:10.3847/1538-3881/ac7da2
- Treu, T., Schmidt, K. B., Brammer, G. B., et al. 2015, *ApJ*, 812, 114. doi:10.1088/0004-637X/812/2/114

Euclid Collaboration, Walmsley, M., et al. 2025,
arXiv:2503.15324.

Wong, K. C., Suyu, S. H., Chen, G. C.-
F., et al. 2020, *MNRAS*, 498, 1420.
doi:10.1093/mnras/stz3094

Euclid Q1 NISP-SIR Gravitational Lens Candidates — Top 8 Gold Complete

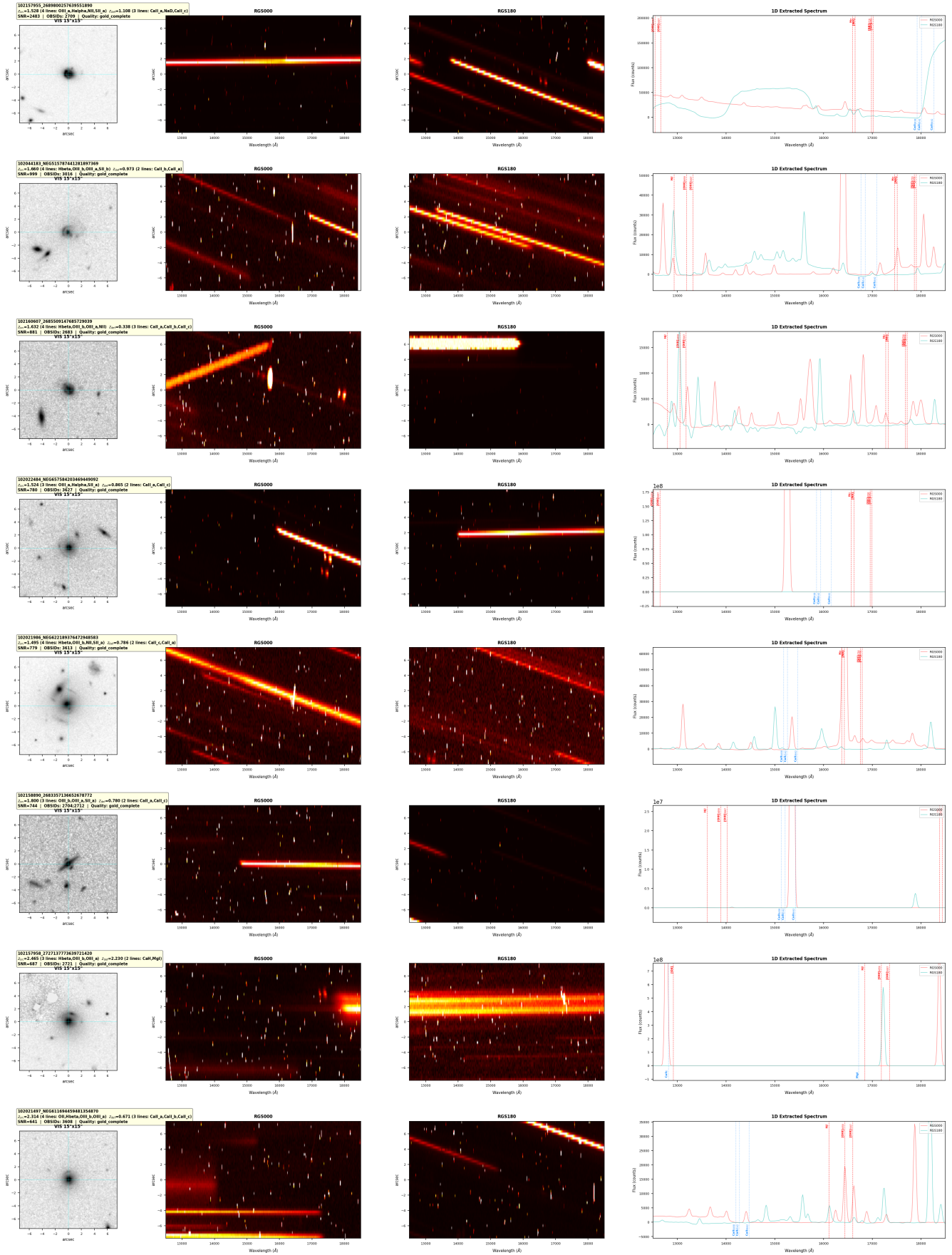


Figure 3: Gallery of the eight highest-SNR gold-complete lens systems, each confirmed in both grism orientations. For each system, four panels are shown: (1) VIS imaging cutout (15" x 15") revealing the lens morphology—arcs, rings, and extended features; (2) 2D SIR spectral stamp from the RGS000 grism; (3) 2D SIR stamp from the anti-parallel RGS180 grism, with the spectral trace visible as a bright diagonal; (4) extracted 1D spectrum with emission lines labeled and redshifted to the rest frame. The top row shows the lens system with the highest SNR, and the bottom row shows the system with the lowest SNR. The systems are identified by their IDs and parameters such as redshift (z), SNR, and quality.

Diverse Lens Systems Across the Redshift Range

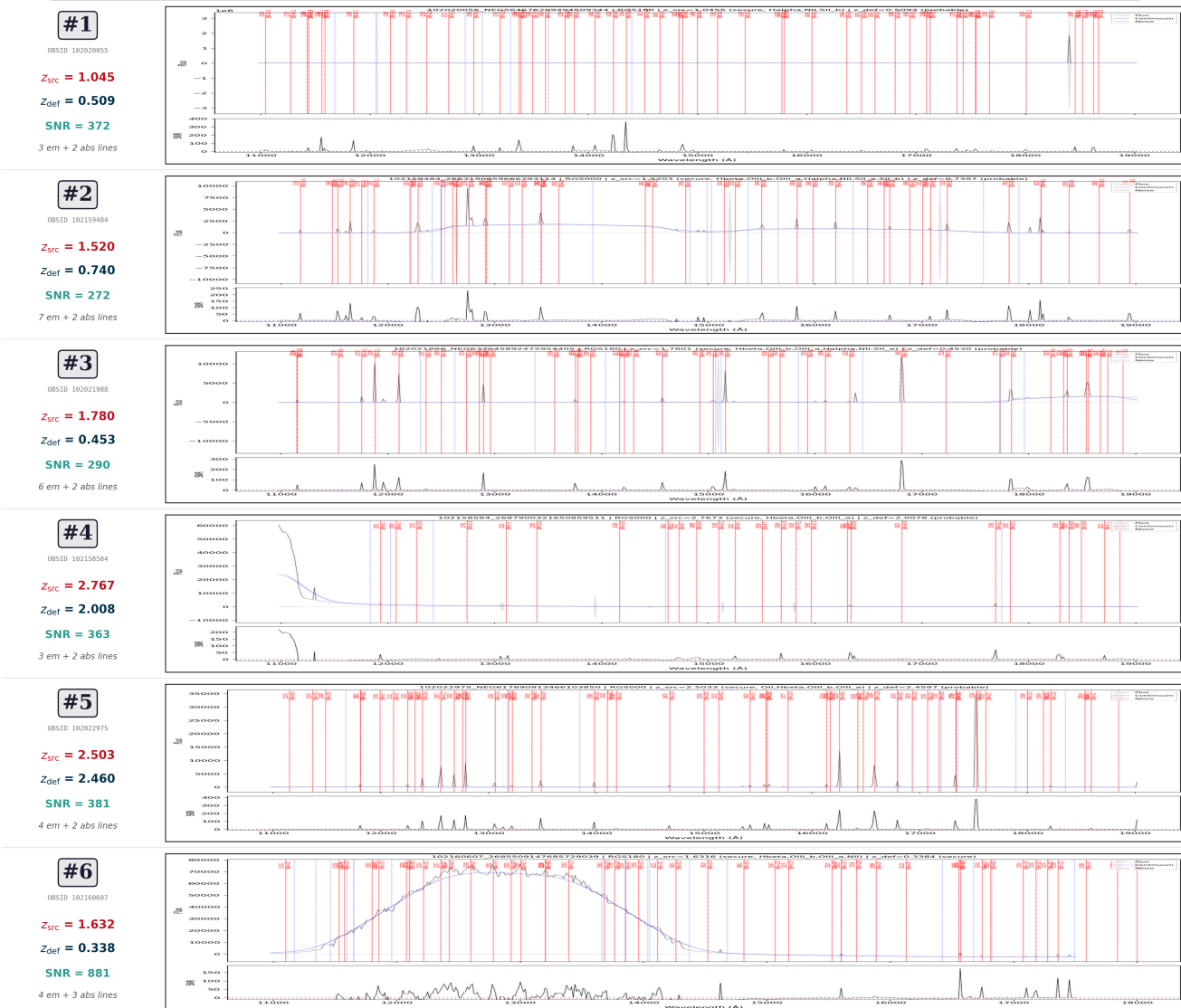


Figure 4: Gallery of six diverse lens systems illustrating the range of source and deflector redshifts, line multiplicities, and spectral morphologies in the catalog. Systems were selected to span the full redshift range covered by NISP, from nearby deflectors ($z_{\text{def}} \sim 0.3$) to high-redshift sources ($z_{\text{src}} > 2.5$).

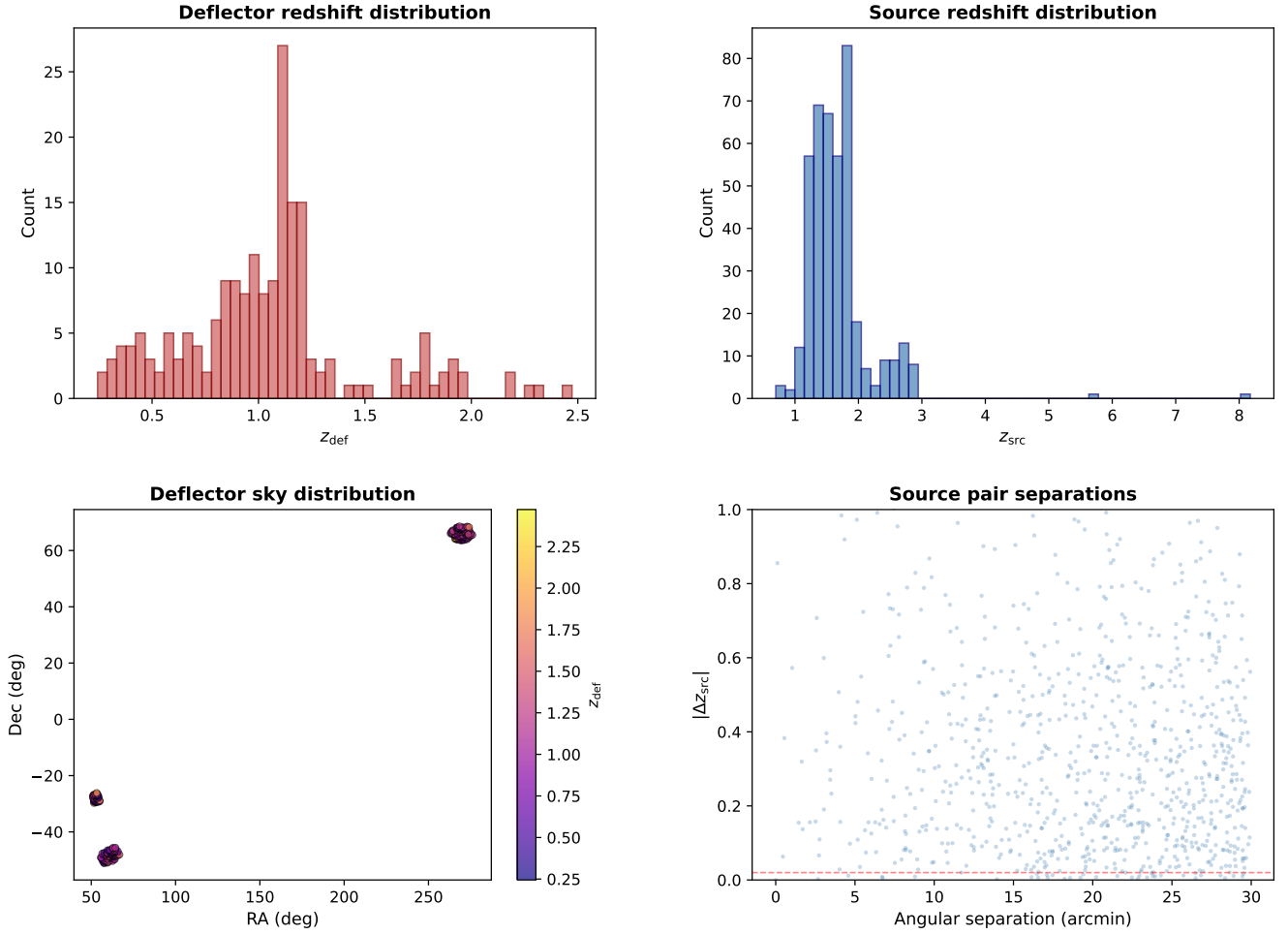


Figure 5: Astrophysical structure in the lens sample. *Upper left:* Deflector redshift distribution with group-scale overdensities at $z \approx 0.93$ (8 systems, red band) and $z \approx 1.10$ (6 systems, orange band) highlighted. *Upper right:* Source redshift distribution with a 3.1σ spike at $z \approx 1.79$ (orange; 23 systems vs. ~ 12 expected from the smoothed baseline, dashed). *Lower left:* Sky positions of deflectors, with the two overdensity groups marked. *Lower right:* Source-pair separations versus $|\Delta z_{\text{src}}|$ for all 1170 pairs within 30 arcmin; 54 pairs with $|\Delta z_{\text{src}}| < 0.02$ (red) trace correlated background structure.

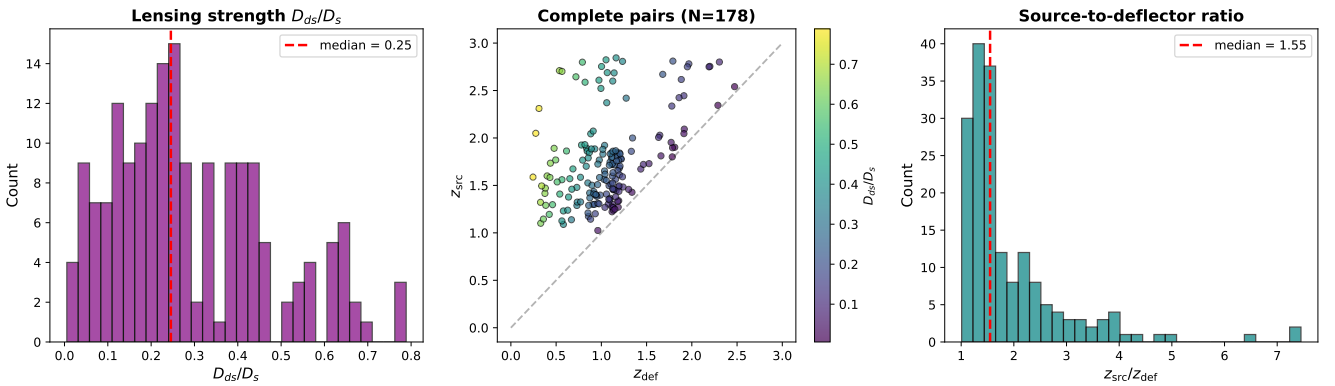


Figure 6: Lensing geometry of the 178 complete pairs. *Left:* Distribution of the lensing strength D_{ds}/D_s ; median = 0.25. *Centre:* Source versus deflector redshift, colour-coded by D_{ds}/D_s . Six systems with $D_{ds}/D_s < 0.05$ (near the identity line) have negligible lensing geometry and are likely misidentifications or projected pairs. *Right:* Distribution of the critical surface density Σ_{cr} .

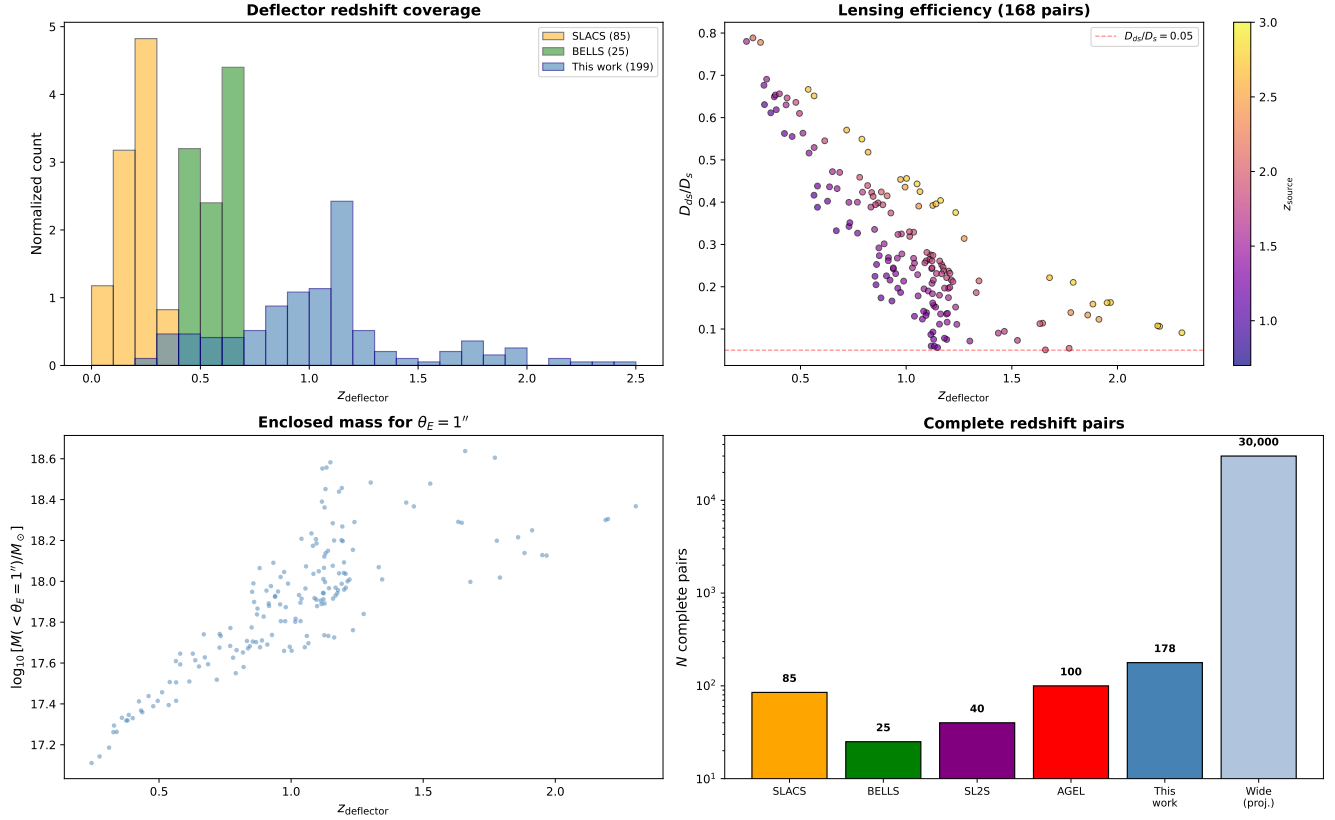


Figure 7: Science potential of the 178 complete redshift pairs. *Upper left:* Deflector redshift distribution compared with SLACS (orange) and BELLS (green); our sample (blue) extends to $z \sim 2.5$. *Upper right:* Lensing efficiency D_{ds}/D_s versus deflector redshift, colour-coded by source redshift. *Lower left:* Enclosed mass within $\theta_E = 1''$ as a function of deflector redshift. *Lower right:* Number of complete (z_s, z_d) pairs across surveys, with the projected Euclid wide survey yield.

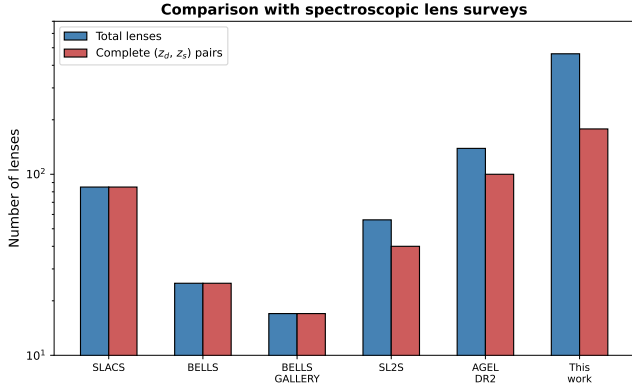


Figure 8: Comparison of spectroscopically characterized lens sample sizes: total lenses (dark bars) and complete sizes: total lenses (dark bars) and complete (z_d, z_s) pairs (light bars). This work (461 total, 178 pairs) exceeds any single prior survey.

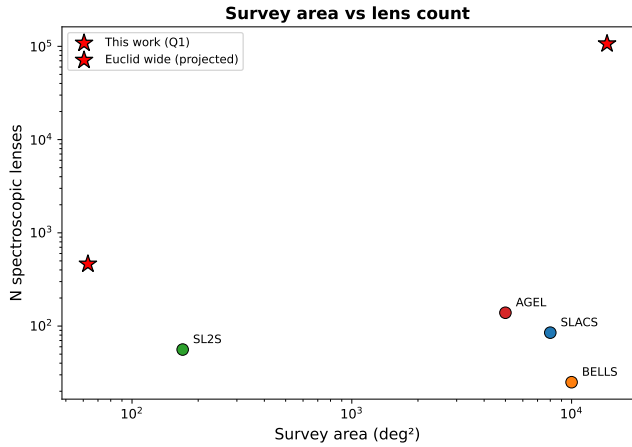


Figure 9: Survey area versus number of spectroscopically characterized lenses. SLACS, BELLS, SL2S, and AGEL are shown as circles; GLASS (cluster lenses) as a triangle. Our Q1 result (filled star) and the projected Euclid wide survey yield (open star) demonstrate the scaling potential of untargeted slitless spectroscopy.